Predicting polyelectrolyte coacervation from a molecularly informed field-theoretic model

My Nguyen,[†] Nicholas Sherck,[†] Kevin Shen,[†] Chelsea E. R. Edwards,[†,‡] Brian Yoo,[¶] Stephan A. Köhler,[§] Joshua Speros,[‖] Matthew E. Helgeson,[†,‡] Kris Delaney,[‡] M. Scott Shell,[*,†] and Glenn H. Fredrickson[*,†,‡,⊥]

[†]*Department of Chemical Engineering, University of California, Santa Barbara, California, 93106, United States*

[‡]*Materials Research Laboratory, University of California, Santa Barbara, California, 93106, United States*

[¶]*BASF Corporation, Tarrytown, New York, 10591, United States*

[§]*BASF SE, Ludwigshafen am Rhein 67056, Germany*

[‖]*California Research Alliance (CARA) by BASF, Berkeley, California 94720, United States*

[⊥]*Department of Materials, University of California, Santa Barbara, California, 93106, United States*

E-mail: shell@ucsb.edu; ghf@ucsb.edu

For Table of Contents use only

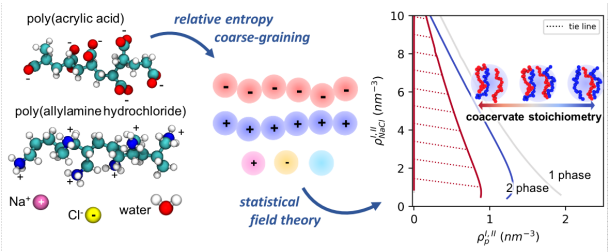

Abstract

Understanding the phase behavior of polyelectrolyte coacervation is crucial for many applications, including consumer formulations, wet adhesives, processed food and drug delivery. However, in most cases, modeling coacervation is not easily accessed by molecular simulation methods due to the long-range nature of electrostatic forces and the typically high molecular weights of the species involved. We present a modeling strategy to study complex coacervation leveraging the strengths of both particle simulations and polymer field theory. Field theory is uniquely suited to capture larger length scales that are inaccessible to particle simulations, but its predictive capability is limited by the need to specify emergent parameters. Using model coacervate forming systems consisting of poly(acrylic acid) (PAA) and poly(allylamine hydrochloride) (PAH), we show an original way to use small-scale, all-atom simulations to parameterize field-theoretic models via the relative entropy coarse-graining approach. The dependence of coacervation on salt concentration, molecular weight and charge stoichiometry are predicted without fitting to experimental data and are consistent with experimental trends including asymmetric phase behavior from non-stoichiometric mixtures of polyelectrolytes. This demonstrates a unique simulation approach to study phase behavior in coacervate forming systems that is particularly useful when chemical specificity is of interest.

1 Introduction

Many technological applications and everyday consumer formulations involve complexation of oppositely charged macro-ions, including processed foods,[1–3] detergent formulations,[4] advanced oil recovery,[5,6] wet adhesives,[7–10] and drug and gene delivery vehicles.[11–14] The complex phase can form in aqueous mixtures consisting any number of natural or synthetic charged species, including synthetic polyelectrolytes, biological polyelectrolytes (e.g., proteins, proteoglycans, polynucleotides), surfactants and colloids, typically in the presence of salt. These mixtures can undergo a liquid-liquid phase separation with the majority of the

oppositely charged macro-ions partitioning into the dense phase, which is referred to as a complex coacervate.[15–18]

The formation of complex coacervates is governed by the complexation free energy with entropic and enthalpic contributions.[19] Experiments suggest one major driving force of coacervation is the entropy gain from counterion release.[20] Although there is a loss in configurational and translational entropy of the macro-ions upon complexation, this contribution is small relative to the counterion entropy in the limit of long polymers. The aforementioned entropic gain as well as the enthalpic driving force due to favorable electrostatic interactions weaken as the salt concentration is increased. Adding salt above a critical concentration leads to the dissolution of the complex coacervate due to the salt's screening of electrostatic interactions.[21,22] Many other variables have been shown to influence coacervation behavior, including the chemical nature of the charged species, stoichiometry, pH, polymer size, and temperature.[18,21,23–26]

The Voorn-Overbeek theory is a classical theory of coacervation that attempts to understand coacervation by approximating the complexation free energy as the combination of the Flory-Huggins mixing entropy and the Debye-Hückle electrostatic energy.[27,28] The theory, however, only captures the mean-field electrostatic environment around individual ions which is only valid in dilute electrolytes (5-10 mM),[29] resulting in quantitative inadequacies at typical coacervate salt concentrations (up to $\sim$ 3 M).[24] Furthermore, polymer charges are treated as unconnected ions; this is an unrealistic depiction of polyelectrolytes that can have high linear charge density. Other theoretical models such as the Edwards approach to polymer field theory properly connect the bound charges to the chain conformations.[30] For such models, the Gaussian approximation (often referred to in the literature as the random phase approximation) is a common analytical method providing the lowest-order perturbation correction to mean-field theory, where the latter is qualitatively inadequate for describing electrostatically driven phase separation.[31–37] Prior studies have shown that the Gaussian approximation captures a significant portion of the fluctuation effects.[36,38–43] At

low charge densities, however, it overestimates the strength of charge correlations and the size of the two-phase region, i.e., the supernatant phase is predicted to be overly depleted of polyelectrolytes by many orders of magnitude.[38,42,44]

Simulations, on the other hand, provide in-roads to probe regimes where analytical techniques cannot push further. Field-theoretic simulations (FTS) utilize the exact statistical field theory to account for field fluctuation effects, which are critical for the study of coacervation.[42,45–47] FTS replaces particle-particle interactions with interactions between individual particles and one or more fluctuating fields, allowing for efficient sampling of configurational integrals over particle configurations. As a result, this simulation method is uniquely suited to the study of high molecular weight and high density charged systems. Moreover, in the field representation the species' chemical potentials are readily available from ensemble-averaged operators without the need for sophisticated, often expensive, free energy techniques required in molecular dynamics (MD) simulations.[48] A range of studies have used FTS to elucidate the effects of charge patterning, electrostatic environment and inclusion of explicit counterions on complex coacervation.[38–43,49]

Despite significant effort by theory and simulation with fine-tuned models beyond the Voorn-Overbeek theory, the asymmetry in coacervation phase diagrams due to the different chemical structures of the involved charged moieties proves difficult to capture accurately. For example, it is often assumed in theoretical models that the polyanion and polycation (as well as the anion and cation) have the same chemical structure except for opposite charges, resulting in nonphysical symmetric phase diagrams with respect to the oppositely charged species.[25,50] In other studies, chemistry-specific effects are simply reduced to parameters such as the persistence length or non-bonded cut-off[51,52] or introduced by including phenomenological parameters associated with coarse-grained potentials (e.g., χ parameters).[53] The latter, although providing chemistry-specific interactions that are consistent with experiments, requires a priori knowledge of the component chemistries and thus is not predictive.

We present here a molecularly informed field-theoretic model of polyelectrolyte coacer-

vation that utilizes a bottom-up coarse-graining approach discussed in our previous work.[54] We build upon our prior work–a multiscale approach to simulating binary water-PEO phase behavior–by introducing more components and electrostatic interactions. In short, the approach leverages the efficiency of the field theory in simulating systems that are large, dense and comprised of high molecular weight species, while providing chemical specificity through small-scale, all-atom (AA) simulations. We derive parameters for the field theory by performing a systematic coarse-graining of representative AA simulations, using a strategy based on the minimization of the relative entropy, S_{rel}.[55–58] The proposed simulation strategy enables efficient calculation of phase diagrams in the field representation while retaining chemical details via systematic coarse-graining of AA simulations. We demonstrate the predictive capability by comparing the phase behavior of a well-characterized model coacervate system consisting of poly(acrylic acid) (PAA) and poly(allylamine hydrochloride) (PAH) in a sodium chloride (NaCl) aqueous solution. PAA, which serves as the polyanion species, has a pK_a of 4.5 while PAH, which is the polycation species, has a pK_a of 8.5.[59,60] Coacervation in a mixture of PAA and PAH is sensitive to the pH, salt concentration, and molecular weight of the polyelectrolytes (PEs).[21,22,24] This sensitivity results from the variable ionization state of the weak PEs and the screening of the long-range electrostatics upon the addition of salt.[61] For the sake of simplicity, we only investigate coacervation in mixtures of fully charged PAA and PAH, corresponding to a pH $\sim$ 6.5, with the PEs having the same degrees of polymerization.

The article is organized as follows: section 2.1 describes the details of the AA simulations and coarse-graining procedure. Section 2.2 discusses our approach to map out the phase diagram. Section 3.1 and 3.2 provide results and discussions on the effect of salt, molecular weight and charged monomer stoichiometry on coacervation. We show a direct comparison to experimental results and provide discussion on the CG model's quality. Section 4 concludes our findings.

2 Computational details and methods

2.1 Reference all-atom systems and bottom-up coarse-graining procedure

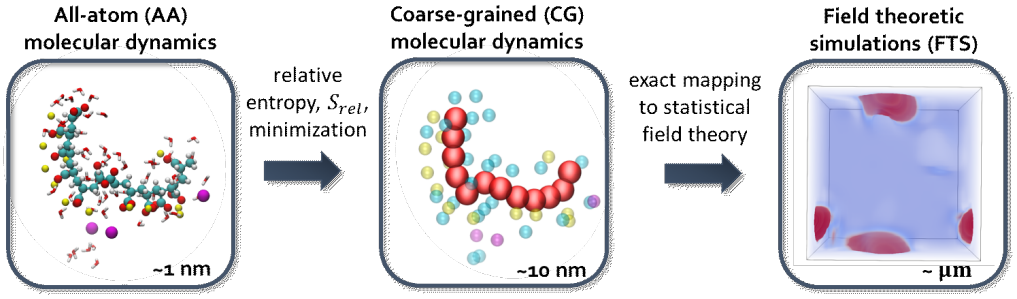

Figure 1: Schematic of the multi-scale simulation workflow that bridges the all-atom and field models.

While we have already outlined the workflow for developing a molecularly-informed field theory in our prior works,[54,62] we briefly discuss the protocol used in this study in the current section as illustrated in Fig. 1. The field-theoretic model is a coarse-grained description of the AA model, and here we define five CG bead types: PAA and PAH monomers, Na^+, Cl^-, and water (Fig. 2). CG sites are generally defined as center-of-mass coordinates of groups of atoms in the AA representation. For the CG model presented in this paper, we use this mapping for each small molecule (water, Na^+ and Cl^-) and each PE monomer, to obtain mapped AA reference trajectories for coarse-graining. Notably, in this work we introduce CG sites that carry explicit fixed-point charges, specifically PAA monomer (p_-), PAH monomer (p_+), Na^+, and Cl^- each carry an integer charge of ± 1.

We use three reference systems to parameterize the CG model: pure water, NaCl aqueous solution, and an aqueous PE-NaCl mixture. We use the Optimal Point Charge (OPC) forcefield for water,[63] and the Joung-Cheatham's forcefield for Na^+ and Cl^- ions.[64] For PAA we use the General Amber Forcefield (GAFF2), while for PAH we use AMBER ff99 forcefield.[65,66] We employ the restrained electrostatic approach to assign atomic fixed-point

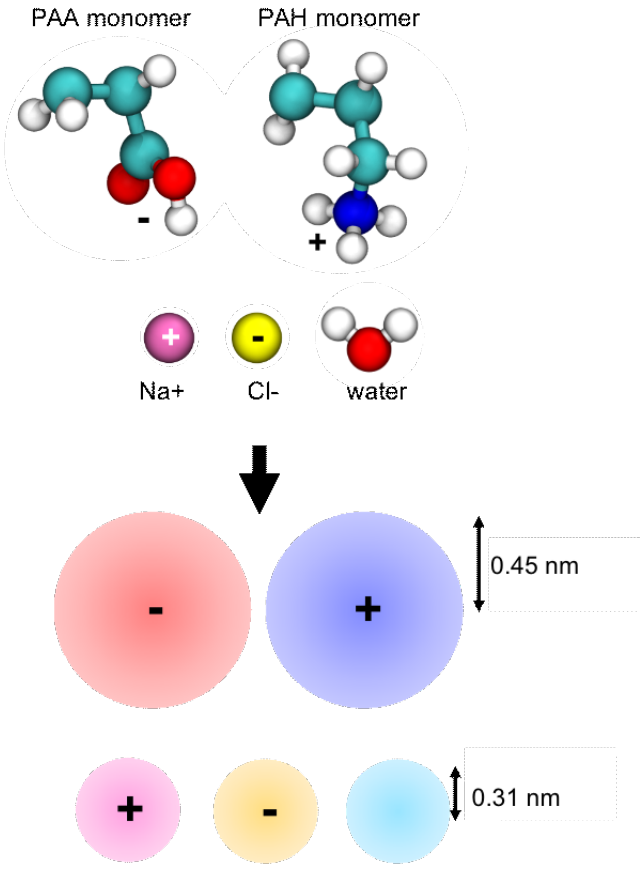

Figure 2: From left to right and top to bottom, the AA-to-CG mappings for PAA monomer (p_-), PAH monomer (p_+), Na^+, Cl^- and water (w). The CG bead radius is 0.45 nm for the PE monomers and 0.31 nm for the small molecules. See main text for details on the coarse-graining procedure.

partial charges for the PEs at the HF6/31G* level in gas-phase calculations using the Gaussian16 software package.[67] We find excellent agreement between aqueous solution densities from simulations and experiments for 45-mer PAA and 187-mer PAH in water at 1 atm and 298.15 K, when compared to experiments with synthetic polymers of matching average molecular weight (Fig. S1). This agreement suggests that this set of forcefield parameters (OPC, Joung-Cheatham, GAFF2, and AMBER ff99) is a reasonable model for the PE mixture.

The physical behavior of the AA system is coarse-grained into mesoscale models amenable to analytical conversion to a field theory. The CG forcefield consists of a harmonic bond

potential

$$\beta U_{b,\alpha}(r) = \frac{3}{2b_\alpha^2} r^2 \tag{1}$$

where $\beta = 1/k_B T$ and b_α is interpreted as the root-mean-square length of a bond for a homopolymer of bead species α. The excluded volume and Coulomb interactions between all site pairs, including bonded pairs, are described by non-bonded pairwise terms involving repulsive Gaussian and regularized Coulomb potentials, respectively:

$$\beta U_{ev,\alpha\gamma}(r) = v_{\alpha\gamma} e^{-r^2/2(a_\alpha^2 + a_\gamma^2)} \tag{2}$$

$$\beta U_{el,\alpha\gamma}(r) = \frac{l_B \sigma_\alpha \sigma_\gamma}{r} \operatorname{erf}\left(\frac{r}{2\sqrt{a_\alpha^2/2 + a_\gamma^2/2}} \right) \tag{3}$$

where $v_{\alpha\gamma}$ describes the excluded volume strength between bead species α and γ, a_α and σ_α are the interaction range and the charge carried by CG-site α, respectively. Here, we set the Bjerrum length, l_B, to 0.74 nm, which is approximately the Bjerrum length of OPC water at 298 K and 1 atm.[63] The regularized Coulomb potential of Eq. 3 reduces to the conventional unscreened Coulomb potential at large separations r, but is finite at contact due to the error function. Such regularization is necessary because of the soft-core repulsions adopted in Eq. 2. The field theory representation of the same coarse, particle-based model is constructed using the Hubbard-Stratonovich-Edwards transformation. This transformation decouples the non-bonded pair interactions such that particles interact only via the bonded potential and with auxiliary fields introduced by the transform.[45] The result is a partition function in terms of integrals over field configurations instead of particle coordinates:

$$\mathcal{Z} \propto \int d\boldsymbol{r}^n \, e^{-\beta U(\boldsymbol{r}^n)} \rightarrow \int \mathcal{D}\boldsymbol{w} \int \mathcal{D}\boldsymbol{\rho} \, e^{-H[\boldsymbol{w},\boldsymbol{\rho}]} \tag{4}$$

where the auxiliary fields $\boldsymbol{w}$ can be viewed as fluctuating chemical potential fields conjugate to fluctuating density fields $\boldsymbol{\rho}$, and H is the effective Hamiltonian that determines the

statistical weight of a field configuration. The form of H is discussed and given in section S3.

As done in our previous work, we enforce specific interaction radii to retain the desired, long-length scale physics without resorting to an aggressive high-resolution AA to CG atom mapping.[54] A convenient choice is the cube-root of the CG beads' specific volumes approximated from AA simulations of pure component for water and single component aqueous solutions for the other components: $a_w = a_{Na^+} = a_{Cl^-} = 0.31\,\text{nm}$, $a_{p-} = a_{p+} = 0.45\,\text{nm}$. We then use S_{rel} minimization to obtain the remaining 17 parameters in the following order: (1) $v_{w,w}$ from a pure water system in the NPT ensemble, (2) v_{w,Na^+}, v_{w,Cl^-}, v_{Na^+,Na^+}, v_{Cl^-,Cl^-}, and v_{Na^+,Cl^-} from NaCl aqueous solution in the external potential ensemble,[62] and lastly, (3) $v_{w,p-}$, $v_{w,p+}$, $v_{Na^+,p-}$, $v_{Na^+,p+}$, $v_{Cl^-,p-}$, $v_{Cl^-,p+}$, $v_{p-,p-}$, $v_{p+,p+}$, $v_{p-,p+}$, b_{p-}, and b_{p+} from the 10 weight % PE-NaCl mixture in the NPT ensemble. Once the parameters are determined, they are fixed in subsequent steps.

The necessary three reference AA simulations are conducted with the OpenMM simulation package.[68] We use a 1 nm cutoff for the direct space non-bonded interactions and use the Particle Mesh Ewald method to compute long range interactions for both Coulomb and Lennard-Jones (LJPME method in OpenMM). In addition, we constrain the length of all bonds that involve a hydrogen atom and employ a time step of $dt = 0.002$ ps. The temperature is set to 298.15 K using the Langevin thermostat with a friction coefficient of 5 ps^{-1}, while the pressure is set to 1 atm using the Monte Carlo barostat with an update frequency of 25 dt. Details on the system size, components, and simulation parameters are provided in SI section S1.2.

With the pure water reference simulation in the NPT ensemble, we parameterize the water-water interaction such that the CG model has a compressibility $\kappa_T \sim 0.062\ k_BT/a_w^3 \sim 4.51 \times 10^{-10}\,\text{Pa}^{-1}$, near that of OPC water. As discussed in our prior studies,[54] matching κ_T between AA and CG simulations uniquely determines the CG pressure of $P_{CG} \approx 8.5\ k_BT/a_w^3$.

We employ an external potential ensemble[62] to determine the self (Na^+ to Na^+ and Cl^-

to Cl^-) and cross-interactions (Na^+ to Cl^-, Na^+ to water, and Cl^- to water) in a salt-water solution. For miscible mixtures, coarse-graining in the external potential ensemble shows improved thermodynamic fidelity and transferability of CG models over the widely used single, uniform-composition ensembles. As detailed in our previous work,[62] the coarse-graining is performed at a state of inhomogeneous response in the composition due to an applied spatially-varying external potential on different species. The resulting CG model is then optimized such that its interactions reproduce the same response as the AA reference system while capturing the dependence on the locally varying composition. Here, we observe improved NaCl mixing thermodynamics in water, evidenced by the mean ionic activity in Fig. S5, when we derive the CG model in the presence of the sinusoidal external potential (visualized in Fig. S2). We choose the optimal external potential ensemble to optimize the CG parameters by maximizing the trace of the Fisher information matrix (the Hessian of S_{rel} with respect to the interaction parameters); we find the maximum in the Fisher information matrix for external sinusoidal potentials to lie near an amplitude of 2 k_BT, Fig. S6.

The last reference simulation is a solution of 10 weight % PEs (50:50 mol/mol PAA to PAH; 24-mers, fully-ionized) and 0.3 M NaCl in the NPT ensemble. We model the PEs as atactic polymers; they are built with the target dyad composition of around 0.44 meso and 0.56 racemic as per the Bernoullian distribution, Fig. S4.[69,70] We note that the CG forcefield is composed of soft interaction potentials that do not account for the bending stiffness that partially dictates the chain conformation in the reference model. Chain conformation embeds information about the bending rigidity, intramolecule interactions, volume exclusion effects, and solvent screening; thus, it is essential for the CG model to reproduce this characteristic of the reference system. We reduce this complex interplay to a simple quantity - the average radius of gyration, R_g, and require the CG model to reproduce the average R_g of PAA and PAH in the reference AA simulation. This constraint is enforced during the S_{rel} minimization by modifying the objective function according to an augmented Lagrangian method:[71–73]

$$F_{obj}(\boldsymbol{x}) = S_{rel}(\boldsymbol{x}) - \lambda \left(\langle R_g \rangle_{CG}(\boldsymbol{x}) - \langle R_g \rangle_{AA} \right) + \frac{c}{2} \left(\langle R_g \rangle_{CG}(\boldsymbol{x}) - \langle R_g \rangle_{AA} \right)^2 \quad (5)$$

where $\boldsymbol{x}$ are the CG forcefield parameters of interest, the coefficient c, typically $\sim \mathcal{O}(10^{10})$, is chosen to bias the CG model's average radius of gyration, $\langle R_g \rangle_{CG}$, towards that of the mapped AA system,$\langle R_g \rangle_{AA}$. The Lagrange multiplier at iteration k is defined as $\lambda_k = \lambda_{k-1} - c\left(\langle R_g \rangle_{CG,k-1} - \langle R_g \rangle_{AA} \right)$. In contrast to neutral polymers, PEs often have long persistence lengths ($\sim$ 10 nm as suggested from our simulations and other works)[74,75] due to the repulsion of backbone charges. Hence, the mismatch in the chain conformation between the CG and AA systems will be significant without considering chain stiffness in the coarse-graining, especially for stiff polymers. We tabulate all forcefield parameters for the CG model and provide them in Tables S1 and S2.

2.2 Multi-component phase boundary calculations

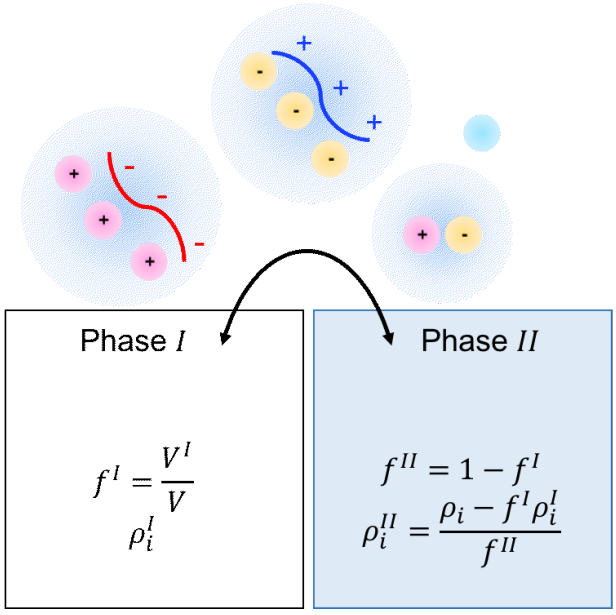

Figure 3: Schematic of the Gibbs ensemble. Coexisting dilute and coacervate phases are partitioned into separate simulation boxes. Neutral pairs of charged molecules ($p-$/Na^+, $p+$/Cl^- and Na^+/Cl^-) and water are exchanged to achieve electrochemical equilibrium and phase volumes are exchanged to achieve mechanical equilibrium.

We determine the multi-component phase equilibrium conditions within the field theory in the Gibbs ensemble where the coexisting phases are partitioned into separate simulation boxes.[76] The overall Gibbs ensemble consists of two subsystems; each is treated in the canonical ensemble, with the distribution of mass and volume in each subsystem being constrained by the overall species densities. At phase coexistence, the overall free energy, F, is minimized and the system is in mechanical and electrochemical equilibrium,

$$\frac{\partial F}{\partial V^I} = -(P^I - P^{II}) = 0 \tag{6}$$

$$\frac{\partial F}{\partial n_m^I} = \mu_m^I - \mu_m^{II} + \sigma_m \Delta\Psi = 0 \tag{7}$$

where V is the simulation box volume, P is the pressure, n_m is the number of molecules m and μ_m is its chemical potential, and the superscript denotes phase I or II. The last term in Eq. 7 accounts for the electrostatic potential difference between the two phases and depends on the charge of molecule m, σ_m, and the Galvani potential, $\Delta\Psi$. Instead of exchanging individual molecular species, we exchange neutral pairs of charged molecules such that the equilibrium condition of Eq. 7 becomes

$$\frac{\partial F}{\partial n_i^I} = \mu_i^I - \mu_i^{II} = 0 \tag{8}$$

where i denotes the following neutral pairs: $p-/\mathrm{Na}^+$, $p+/\mathrm{Cl}^-$ and $\mathrm{Na}^+/\mathrm{Cl}^-$, in addition to water. We note that $n-1$ linearly independent neutral pairs are sufficient to span all possible values of $n-1$ independent densities in a system of n charged species. We define the effective chemical potentials of the neutral pairs from the chemical potentials of the charged

molecules as

$$\mu_{p-/Na^+} = \mu_{p-} + N_{p-}\ \mu_{Na^+} \tag{9}$$

$$\mu_{p+/Cl^-} = \mu_{p+} + N_{p+}\ \mu_{Cl^-} \tag{10}$$

$$\mu_{Na^+/Cl^-} = \mu_{Na^+} + \mu_{Cl^-} \tag{11}$$

where N_{p-} and N_{p+} are the degrees of polymerization of PAA and PAH, respectively, and μ_i are the *per molecule* chemical potentials. The mass balance gives the expression for the overall monomer density of pair i

$$\rho_i = f^I \rho_i^I + f^{II} \rho_i^{II} \tag{12}$$

where the volume fractions of phase I is $f^I = V^I/V$ and phase II is $f^{II} = 1 - f^I$. Equilibrium is achieved by performing mass and volume swaps between the simulation boxes formulated as the following differential equations in a fictitious time t

$$\begin{aligned} \frac{df^I}{dt} &= P^I - P^{II} \\ \frac{d\rho_i^I}{dt} &= -(\mu_i^I - \mu_i^{II}) \end{aligned} \tag{13}$$

In practice, we conduct a series of iterative simulations. In each iteration, we perform two separate canonical simulations that represent phases I and II. We update the volume fractions and species' densities with the following scheme until the equilibrium conditions,

Eq. (6),(8), are satisfied:

$$\rho_{tot}(k+1) = \rho_{tot}(k) - \Delta t_{\rho_{tot}}(P^I - P_{CG}) \tag{14}$$

$$f^I(k+1) = f^I(k) + \Delta t_f \left(P^I(k) - P^{II}(k)\right) \tag{15}$$

$$\rho_i^I(k+1) = \rho_i^I(k) - \Delta t_{\rho_i} \left(\mu_i^I(k) - \mu_i^{II}(k)\right) \tag{16}$$

$$f^{II}(k+1) = 1 - f^I(k+1) \tag{17}$$

$$\rho_i^{II}(k+1) = \frac{\rho_i - f^I(k+1)\rho_i^I(k+1)}{f^{II}(k+1)} \tag{18}$$

where k is the discrete time index, Δt_f, $\Delta t_{\rho_{tot}}$, and Δt_{ρ_i} are step sizes for volume fraction, overall density, and species density swaps, respectively. Eq. 14 updates the overall bead density, $\rho_{tot} = \sum_{m\in[p-,p+,Na^+,Cl^-,w]} \rho_m$, at fixed overall species fractions such that the coexisting phases will be at the pressure of the CG model, P_{CG}. This condition emulates the experimental conditions at constant temperature and pressure. We find that $\Delta t_{\rho_{tot}} = 0.002$, $\Delta t_f = 0.01$ and $\Delta t_{\rho_i} = 0.1\min(\rho_i^I, \rho_i^{II})$ work well. From our definitions of neutral pairs, the bead density for each charged species follows as

$$\rho_{p-} = \rho_{p-/Na^+} \tag{19}$$

$$\rho_{p+} = \rho_{p+/Cl^-} \tag{20}$$

$$\rho_{Na^+} = \rho_{p-/Na^+} + \rho_{Na^+/Cl^-} \tag{21}$$

$$\rho_{Cl^-} = \rho_{p+/Cl^-} + \rho_{Na^+/Cl^-} \tag{22}$$

To rapidly screen phase behavior, we use a Gaussian approximation to evaluate the pressure and chemical potentials used in field-theoretic Gibbs ensemble simulations. Previous efforts have shown that the Gaussian approximation, while it only includes field fluctuations up to second order, is semi-quantitative in reproducing the dense branch of the coacervate phase diagram.[38,40,41] Specifically in our work, we add Gaussian fluctuation modes of the electrostatic interactions on top of a mean-field treatment of excluded-volume interactions.

The analytical expressions for the requisite thermodynamic quantities are provided in section S3.

3 Results and discussion

3.1 Polyelectrolyte mixture with no added salt

Prior experiments have suggested that the propensity for coacervation decreases with the degree of non-stoichiometry in charged monomer compositions.[21,22] We probe the effect of charged monomer stoichiometry in a salt-free mixture consisting of PAA, PAH, the appropriate ion needed to neutralize the system, and water. The amount of PAA relative to PAH in the mixture is controlled by the PAA fraction parameter defined as $f_{p-} = \rho_{p-}/\rho_p$ where $\rho_p = \rho_{p-} + \rho_{p+}$ is the total bead number density of the PEs. The bead density of PAH is thus $\rho_{p+} = (1 - f_{p-})\rho_{p-}/f_{p-}$. When $f_{p-} > 0.5 (< 0.5)$, PAA (PAH) is in excess and we include Na^+ (Cl^-) to neutralize the system.

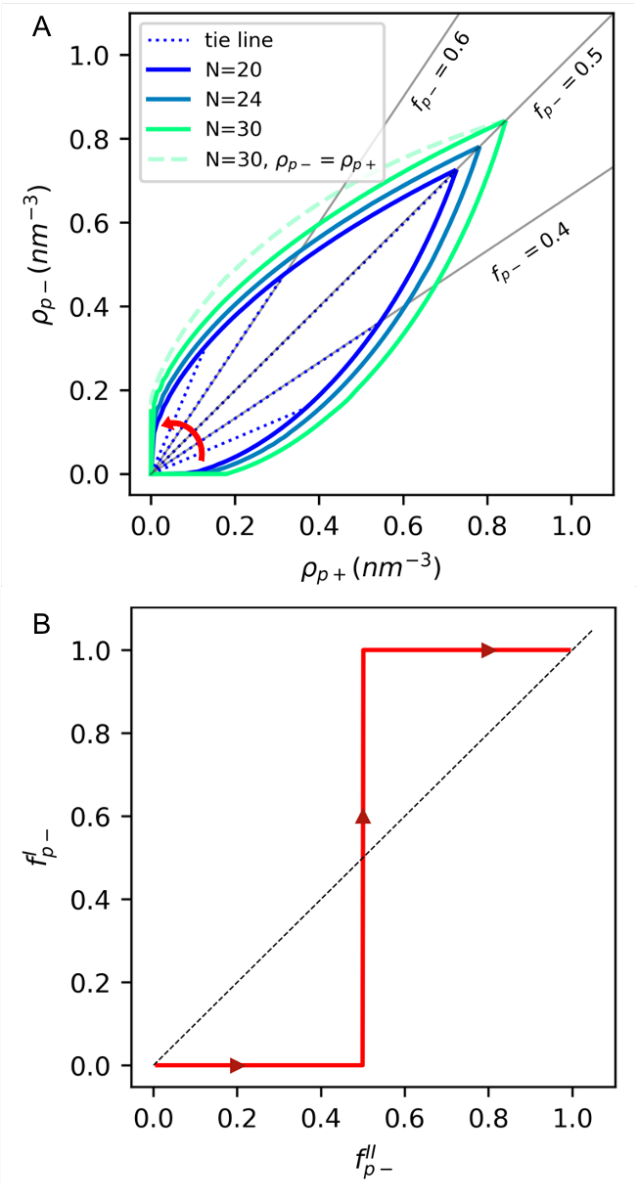

Figure 4: (A) Phase diagram for the salt-free condition of a PAA/PAH mixture at varying chain length, N. The solid lines denote the binodals and dotted lines are example tie lines. Gray solid lines represent compositions corresponding to specific f_{p-} values, as annotated on the figure. The faded dashed line is the hypothetical binodal for excess PAA conditions at $N = 30$ if the phase diagram is symmetric ($\rho_{p-} = \rho_{p+}$). The red arrow shows a path traversing from a PAH-rich mixture ($f_{p-} \to 0$) to a PAA-rich mixture ($f_{p-} \to 1$) for $N = 20$. (B) A plot of the monomer fraction of PAA in the coexisting dilute, f^{I}_{p-}, and coacervate phases, f^{II}_{p-}, along this path at $N = 20$.

Fig. 4A shows the binodals for the PE chain lengths $N = 20$, 24 and 30. The tie line, connecting the compositions in the dilute and coacervate phases, shortens with increasing

deviation from charged monomer stoichiometry. The stoichiometric condition is denoted by the diagonal line, whereas other stoichiometries are gray lines above ($f_{p-} > 0.5$) or below ($f_{p-} < 0.5$) the diagonal. The increased propensity for coacervation with increasing N is reflected by both longer tie lines (evident at $f_{p-} = 0.5$) and larger range of composition enclosed by the binodal.

For values of N shown here, the alignment of tie lines and the stoichiometry lines suggest that the coacervate retains the overall stoichiometry. This also indicates that most of the excess PEs go into the coacervate phase (with the excess charges being neutralized by the counterions) while the dilute phase is almost devoid of both species of PE. This observation of the coacervate's stoichiometry relative to the overall mixture's is qualitatively different from previous theoretical work by Zhang et al.[25] In their work, the tie lines are almost parallel to the diagonal line, suggesting the that the PEs re-distribute in the coexisting phases such that the coacervate phase composition is less asymmetric in terms of the number of oppositely charged monomers as compared to the overall mixture. These differences could be the results of the enhanced charged connectivity in the Gaussian approximation of the field theory and chemical specific interactions that we employ here.

For the dilute phase, it is more illustrative to show the trajectory of the stoichiometry in the coexisting dilute phase (phase I) and coacervate phase (phase II), Fig. 4B, as we follow the path traversing across tie lines starting from $f_{p-} \to 0$ to $f_{p-} \to 1$ (red arrow in Fig. 4A). While the PAA fraction in the coacervate phase varies continuously from 0 to 1, this value is either near 0 for $f_{p-} < 0.5$ or near 1 for $f_{p-} > 0.5$ in the dilute phase, suggesting that the dilute phase, while being depleted of PEs, is composed of mostly the PE species in excess. It is also inferred from Fig. 4B that the coacervate is stabilized for all range of stoichiometry, even at $f_{p-} \to 0$ and 1. We hypothesize that the stability of the coacervate over the full range of stoichiometry is due to the parameterization of the coarse-grained PE models at the phase separated state (at $f_{p-} = 0.5$ and 0.3 M NaCl). Interaction parameters derived from this reference state are biased toward the collapsed configurations of PAA and PAH that

promote phase separation even when only one PE species is present. This is related to the transferability of the PE model across stoichiometries which can be improved by employing the external potential ensemble in the parameterization step of the PE-NaCl mixture.

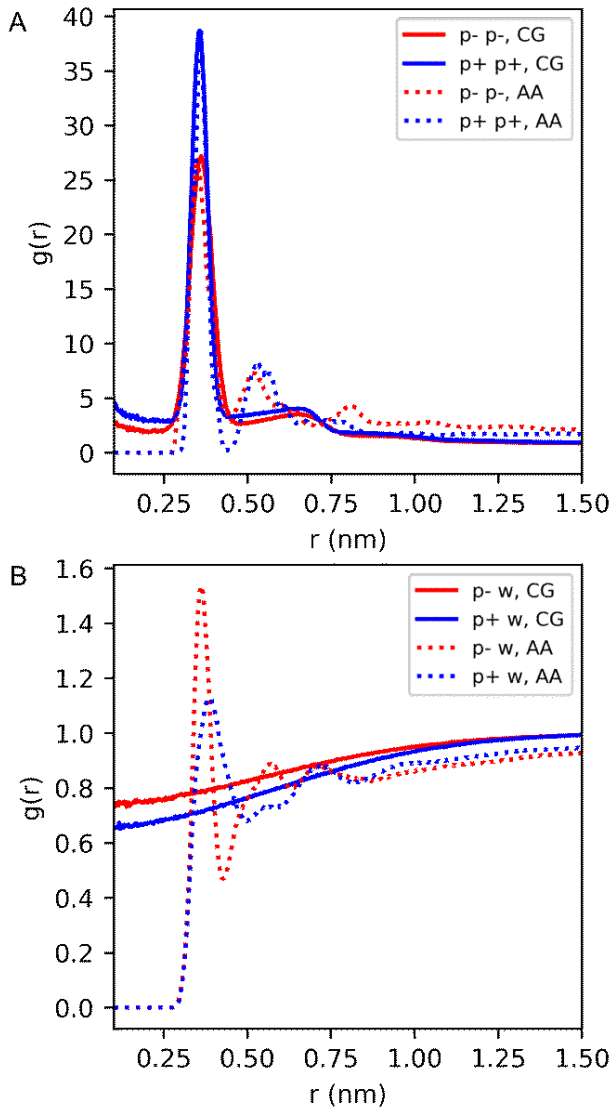

Figure 5: Radial distribution functions (RDFs) between the center-of-mass of the PE monomers and (A) that of the same PE species and (B) water in the CG simulation (solid lines) and the AA simulation (dotted lines). Red and blue lines correspond to PAA and PAH monomers, respectively. The simulation composition is that of the third AA reference simulation discussed in section S1.2.3. The CG models do not retain liquid structuring of the AA model due to our choice of large interaction radii that only resolves long length-scale physics.

Lastly, we want to note that the phase boundaries are not symmetric across the diagonal;

comparing actual phase boundaries to hypothetical boundaries by assuming $\rho_{p+}^{I,II} = \rho_{p-}^{I,II}$ clearly shows the asymmetry (faded dashed lines in Fig. 4A and Fig. S7). The coacervate dense phase incorporates slightly more PAH in non-stoichiometric mixtures with excess PAH (e.g., $f_{p-} = 0.3$), as compared to the incorporation of PAA when it is in excess by the same amount (e.g., $f_{p-} = 0.7$). The tendency of PAH to form a denser coacervate is explained by the radial distribution functions (RDFs) in a mixture of 10 wt % PAA and PAH at $f_{p-} = 0.5$ and 0.3 M NaCl (the composition of the third reference AA system discussed earlier). The analysis of the CG model shows that the PAH monomer-PAH monomer RDF has higher intensity than the PAA monomer-PAA monomer RDF (Fig. 5A) while the PAH monomer-water RDF shows less pronounced structuring than the PAA monomer-water RDF (Fig. 5B). This suggests that PAH is less soluble in water; the same trend is observed in the AA model (dotted lines). This asymmetry arises from the chemistry embedded in our model that leads to different interaction parameters among the charged moieties.

3.2 Polyelectrolyte mixture with added salt

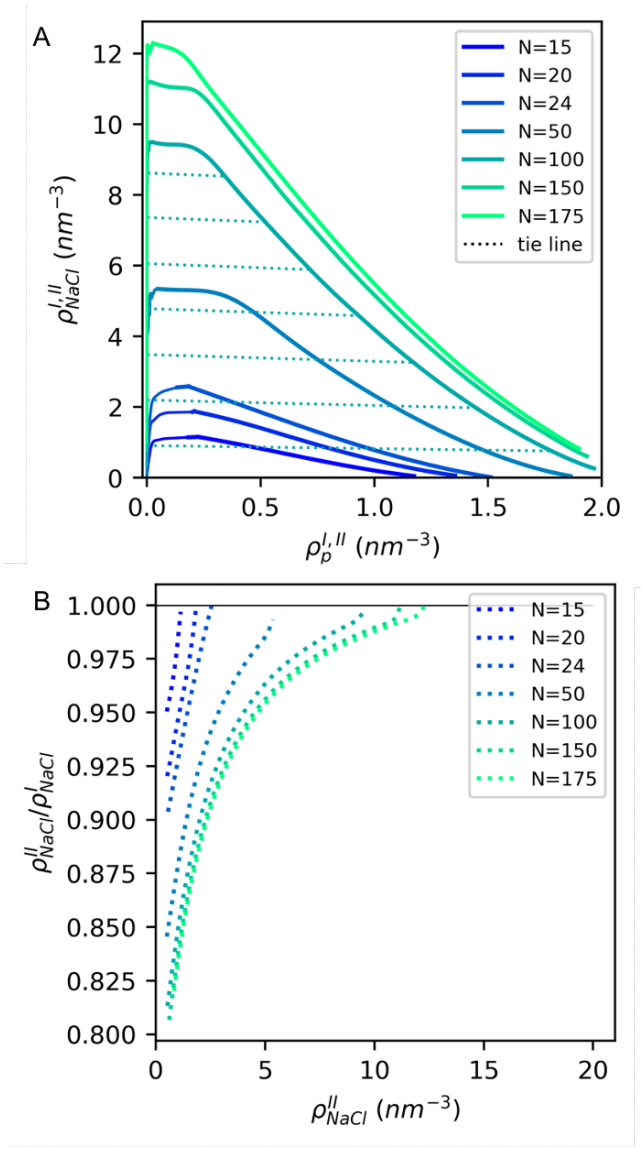

Figure 6: (A) Binodals at $f_{p-} = 0.5$ for varying N. Dotted lines are tie lines for $N = 100$. The negative slope in the tie lines suggests that there is slightly more salt in the dilute phase than in the coacervate phase. This is more evident in (B), a plot of the ratio of salt concentrations in the coacervate phase and the dilute phase as a function of the excess salt concentration in the coacervate. The ratio is always below unity for any values of added salt concentration and N.

We now consider the addition of salt in a PE mixture where the ions stem from both the counterions (one counterion per PE charge) and added salt, i.e., $\rho_{Na^+} = \rho_{p-} + \rho_{salt}$ and

$\rho_{Cl^-} = \rho_{p-} + \rho_{salt}$. Since the small ions have different partitioning behavior in the coexisting phases, we report their concentration in each phase as the smaller value of the Na^+ and Cl^- concentrations, i.e., $\rho^{I,II}_{NaCl} = \min\left(\rho^{I,II}_{Na^+}, \rho^{I,II}_{Cl^-}\right)$; this is equivalent to assessing the excess salt in each phase.

Fig. 6A shows how the dense branch concentration of the two-phase coexistence region for the stoichiometric mixture reduces with salt concentration. The dilute branch concentration, on the other hand, becomes denser with added salt (Fig S8) as the binodal region shrinks from both sides. Increasing salt concentration reduces the effective electrostatic strength due to screening from the increased charge density. Both the entropic and enthalpic driving forces for coacervation diminish with increasing ionic strength before coacervation is thermodynamically unfavorable, at which point the complexation free energy becomes zero (Fig. S9). The salt concentration at this transition, ρ^*_{salt}, characterizes the salt resistance of the coacervates, i.e., the minimum amount of salt to dissolve the coacervate phase. The two-phase region also has a lower bound at $N \sim 15$ and increases with molecular weight until approximately saturating above $N \sim 150$. The higher solubility of shorter PEs is not surprising and is a result of their increased translational entropy and weaker electrostatic correlation energy.[38]

The negatively sloped tie line suggests the excess salt concentration in the dilute phase is slightly higher than in the coexisting coacervate phase. This is readily apparent from the ratio of the salt concentration in the coacervate phase with respect to the dilute phase in Fig. 6B, which is less than unity for all salt concentrations; observations that are consistent for the individual anion and cation species are shown in Fig. S10. As salt is increased at constant N, or as N is decreased at constant ρ^{II}_{NaCl}, the PE concentration in the coacervate phase decreases. This reduces the excluded volume asymmetry between the two phases the salt partitioning ratio increases from values less than 1 towards 1. While experimental efforts have shown the salt partitioning behavior is not universal and depends on other factors such as the chemistry of the PE and charge density,[77,78] our prediction of higher salt partitioning

in the dilute phase is consistent with the experimental observations for the stoichiometric PAA/PAH mixture.[24,79]

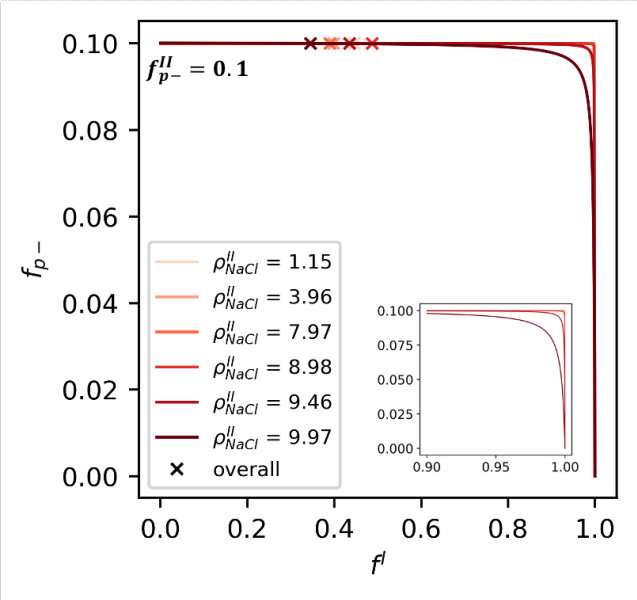

Figure 7: The overall PE stoichiometry f_{p-} along a tie line by varying the dilute phase volume fraction f^I for the case of the coacervate stoichiometry of 0.1. Different series represent tie lines corresponding to different excess salt concentrations in the coacervate (in nm^{-3}). Cross symbols denote the overall compositions used in Gibbs ensemble calculations to obtain the coexisting phases. Inset: expanded region near the dilute phase to highlight the continuous transition of the stoichiometry from 0.1 to 0 at moderate to high salt concentrations.

Using the same protocol, we construct phase diagrams for $N = 150$ at non-stoichiometric conditions. Although in general the stoichiometry of the coacervate phase can be different from that of the initial mixtures and depends on the overall composition, we find that the coacervate maintains the overall stoichiometry and this observation is mostly independent of the overall composition. As a demonstration, for a pair of the coexisting phases we calculate the overall stoichiometry of different mixtures with overall compositions at different points along the tie line by varying the dilute phase volume fraction f^I, which controls the relative proportion of the two phases. The overall stoichiometry along the tie line for the coacervate stoichiometry $f_{p-}^{II} = 0.1$ is presented in Fig. 7 where different series represent tie lines at different salt concentrations. The overall stoichiometry, f_{p-}, approaches the coacervate (dilute phase) stoichiometry as the dilute phase volume fraction approaches 0

(1). At low salt concentrations, the stoichiometry along the tie line is the same as that of the coacervate phase and has a discontinuity at the dilute phase ($f^I = 1$). At moderate to high salt concentrations, the stoichiometry varies continuously from 0.1 to 0 as we approach the dilute phase. This transitional region is indeed quite narrow and appears very close to the dilute phase ($f^I \gtrsim 0.8$) for all stoichiometries we investigated (Fig. S11), suggesting most compositions enclosed by the binodals of Fig. 8A have the same stoichiometry as that of the corresponding coacervate phase. This is expected because the dilute phase has very low concentrations of PE and contributes very little to the overall polymer mass. Going forward, we refer to "non-stoichiometric" mixtures as those with the coacervate phase at non-stoichiometric conditions.

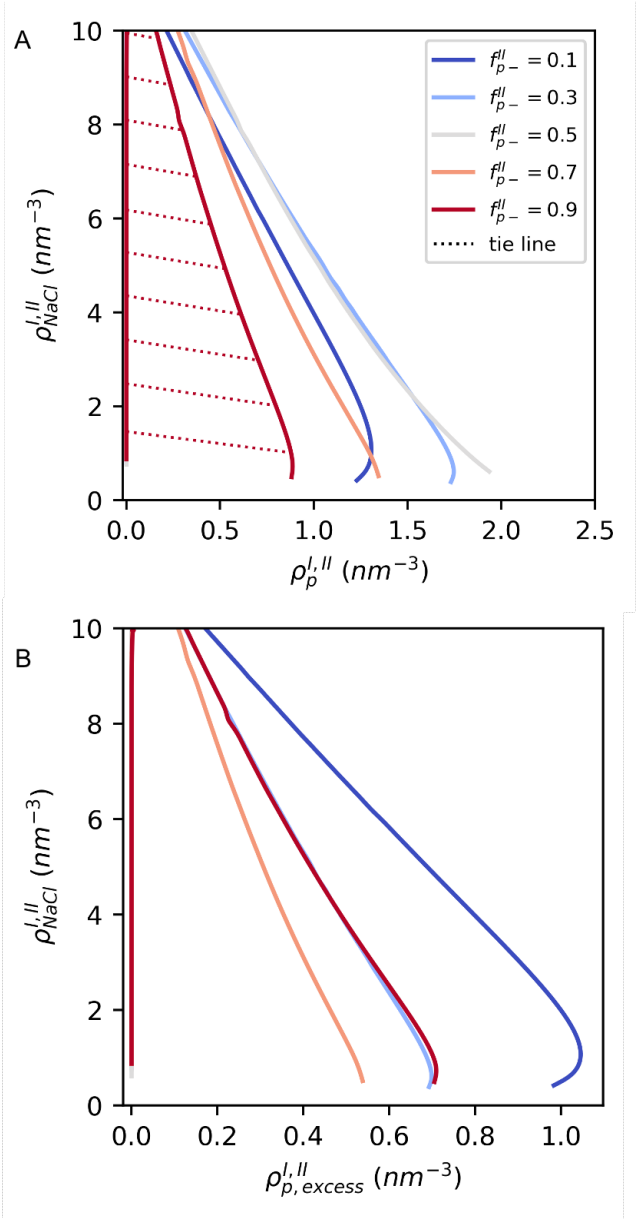

Figure 8: (A) Binodals for $N = 150$ at stoichiometries $f^{II}_{p-} = 0.1, 0.3, 0.5, 0.7, 0.9$ with dotted lines denoting tie lines. The reduced number of potential ion pairs in non-stoichiometric mixtures leads to the shrinkage of the coacervation region. (B) The same salt concentration versus the excess PE concentration $\rho_{p,excess} = |\rho_{p-} - \rho_{p^+}|$ in the coexisting phases; $\rho_{p,excess}$ is essentially zero for the stoichiometric mixture.

Notably, the coacervation regions for non-stoichiometric mixtures are smaller than stoichiometric mixtures as evident in Fig. 8A. At the same overall PE concentration ρ_p, more asymmetric mixtures have fewer potential ion pairs. Thus, less salt is needed to screen the electrostatic interactions and dissolve the coacervate as compared to the stoichiometric con-

dition. Unlike in the stoichiometric mixture, cations and anions have different partitioning behavior in non-stoichiometric mixtures (Fig. 9) due to the electroneutrality constraint: excess PAA (PAH) coacervate require excess Na^+ (Cl^-) in the same proportion to neutralize the charge. For $f_{p-}^{II} = 0.5$, the coacervate phase has equimolar amounts of oppositely charge monomers such that the small ions have freedom to partition in the dilute phase where it is less crowded. We show in Fig. 10 the partitioning ratio of "free ions" that are not neutralizing the excess PEs and have concentration $\rho_{free\ ion}^{I,II} = \rho_{Na^+}^{I,II} + \rho_{Cl^-}^{I,II} - \rho_{p,excess}^{I,II}$. This characterizes the degree of ion partitioning after accounting for the partitioning due to neutralizing the excess PEs in both phases. As expected, when the PE complex is sufficiently neutralized, small ions preferentially partition in the dilute phase.

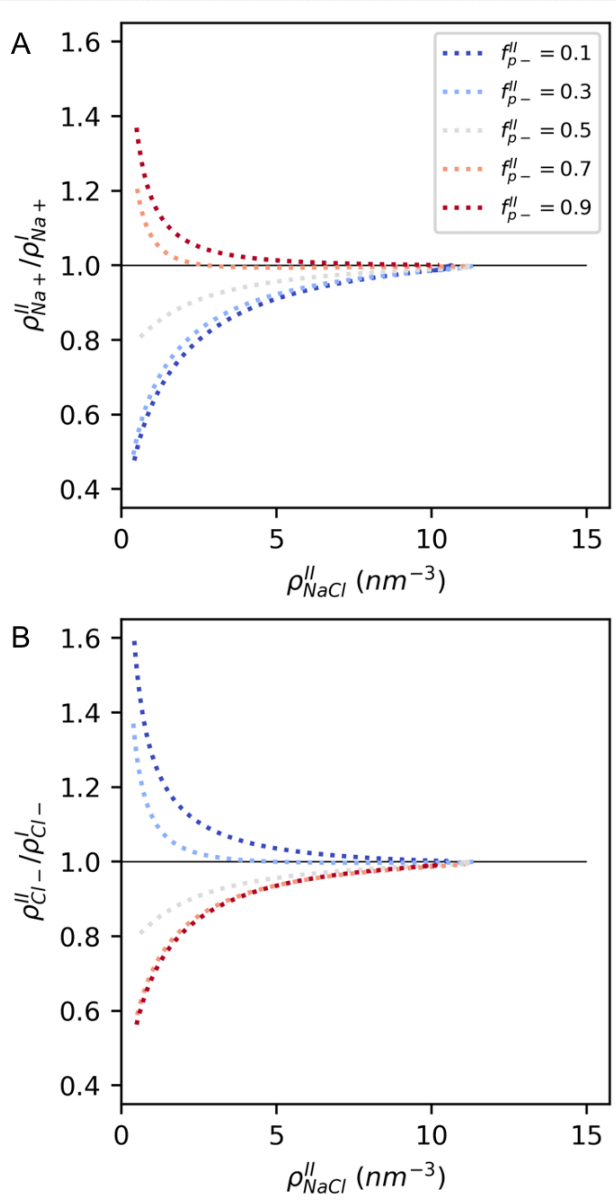

Figure 9: Partitioning ratios of (A) Na^+ and (B) Cl^- across excess salt concentrations in the coacervate for different f^{II}_{p-} at $N = 150$.

Interestingly, at non-stoichiometric conditions the dense branch shows a looping-in shape that has been observed experimentally in other non-stoichiometric PE systems.[77] This looping-in feature is representative of a salting-out phenomenon, where a homogeneous solution undergoes phase separation upon an initial addition of salt.[80] Friedowitz et al. attribute the looping-in feature in their phase diagrams to the competition of the counterion mixing en-

tropy and the electroneutrality constraint in the coacervate when there is charge asymmetry. They argue that when excess PEs preferentially partition into the coacervate, as is observed in our system, salt ions that are not participating in neutralizing the complex preferentially populate the dilute phase to maximize their translational entropy. Consequently, the PE concentration in the coacervate must increase in order to maintain the osmotic pressure balance between the two phases. With sufficient added salt, the salt partitions more evenly across the two phases, and eventually the screening effect dominates, leading to a decrease in coacervate concentration with increasing salt. Fig. 10 shows a drastic decrease in the free ion partitioning ratio for non-stoichiometric mixtures as compared to the stoichiometric condition, especially at low added salt concentrations, which is consistent with the earlier argument of the increased accumulation of free ions in the dilute phase. Furthermore, the salt concentration where the free ion partitioning ratio crosses ~ 0.8 (the partitioning of the $f_{p-} = 0.5$ mixture at low salt) is qualitatively where the looping-in feature ends, suggesting the looping-in shape in the dense branch is indeed related to the partitioning behavior of small ions.

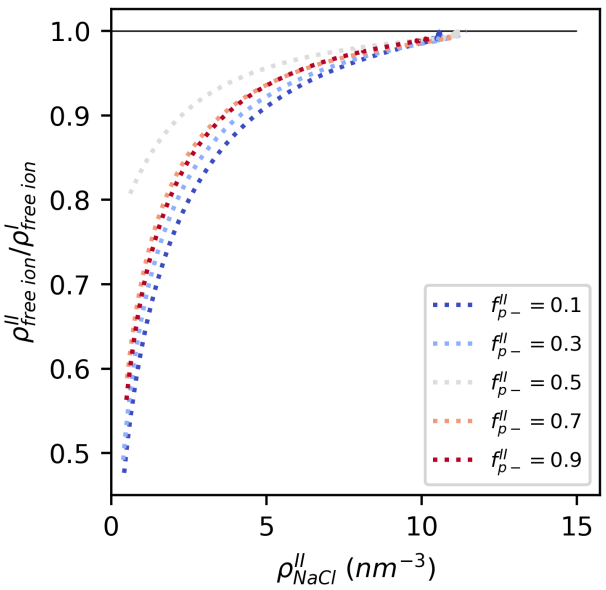

Figure 10: Partitioning ratios of the free ions, $\rho^{I,II}_{free\ ion} = \rho^{I,II}_{Na^+} + \rho^{I,II}_{Cl^-} - \rho^{I,II}_{p,excess}$, across excess salt concentrations for different f^{II}_{p-} at N=150. At low added salt concentrations, this ratio is significantly lower in non-stoichiometric mixtures as compared to stoichiometric mixtures.

Similar to the salt-free condition, we note that the change in the coacervation region is not symmetric between the excess PAA ($f_{p-}^{II} > 0.5$) and excess PAH ($f_{p-}^{II} < 0.5$) conditions. Specifically, the two-phase window for the excess PAH is larger than the excess PAA case at the same degree of non-stoichiometry (e.g. $f_{p-}^{II} = 0.1$ versus 0.9, 0.3 versus 0.7, etc.). In addition, the PE complex carries more charge, characterized by the excess PE concentration $\rho_{p,excess}^{II} = |\rho_{p-}^{II} - \rho_{p^+}^{II}|$, in the case of excess PAH conditions relative to excess PAA conditions at the same ionic strength (Fig. 8B); thus, more counterions (Cl^- for $f_{p-}^{II} < 0.5$, Na^+ for $f_{p-}^{II} > 0.5$) are needed to neutralize coacervates with excess PAH (Fig. 9). Lastly, it is inferred that the propensity for coacervation at a fixed degree of non-stoichiometry is higher when the excess species is PAH than when it is PAA. A similar observation is suggested by the experimental ternary phase diagrams at moderate salt concentrations by Chollakup et al. where the critical stoichiometry, beyond which coacervation does not occur, appears to be biased toward mixtures with higher degree of excess PAH.[21] The fact that we can predict this asymmetry provides some validation of the workflow's ability to preserve the chemical specificity of the AA model in the CG model.

The phase diagram from the Gaussian approximation for $N = 150$ at 1:1 stoichiometry is directly compared to experimental results of the similar system reported by Li et al. and Luo et al. at pH = 6.5 (Fig. 11).[24,79] While qualitatively capturing the screening effect of added salt, the phase diagram shown here: 1) overestimates the critical salt concentration; and, 2) underestimates the PE compositions in the coacervate phase. Deficiency 1) is largely attributable to the Gaussian approximation which neglects higher-order fluctuations that become more important near the critical point (can be resolved by including fields other than the electrostatic potential). From a limited number of particle-based MD simulations of coacervates in equilibrium with a supernatant phase (circles in Fig. 11), we show that with full incorporation of fluctuations the CG model indeed has a comparable salt resistance with experiments and becomes homogeneous above $\rho_{NaCl} \sim 4.5$ nm^{-3}.

In contrast, the underestimation of the coacervate phase polymer density is attributed

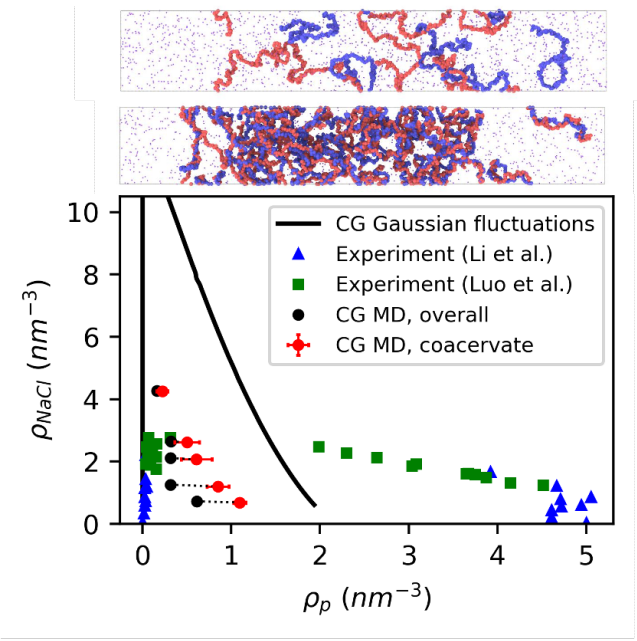

Figure 11: Phase diagrams for stoichiometric mixutures at $N = 150$ from the Gaussian approximation (black line) and CG MD (circles) compared to the experimental data by Li et al. (triangles) and Luo et al. (squares).[24,79] MD simulations are conducted in the NPT ensemble at 298.15 K and P_{CG} in rectangular box of dimensions $\sim 11 \times 11 \times 80$ nm^3. Red circles reflect the PE and salt compositions in the coacervate while black circles are the overall compositions. The PE composition in the dense branch from CG MD approaches the bulk with increasing salt concentration much faster than the Gaussian approximation. The two simulation snapshots from CG MD, showing PAA (red chains) and PAH (blue chains), correspond to the highest (top) and lowest (bottom) salt concentrations shown here; water molecules are not shown for clarity.

to the assumption of a constant dielectric screening effect of the solvent with added salt and PE. The current CG model assumes the Bjerrum length of pure water throughout the coexisting regions while in reality the Bjerrum length is likely larger in the dense coacervate (corresponding to smaller dielectric constant). With an increased Bjerrum length, the attractive interactions between PE monomers will be stronger, resulting in more concentrated coacervate branch. A more sophisticated model that better describes the actual electrostatic environment would be one with a dielectrically active solvent. Specifically, one can model the solvent as a polarizable or fixed-dipole solvent such that the screening depends on the local environment;[81] we leave investigating such a model to future work.

A potential further refinement to the workflow would be to coarse-grain the PEs-PEs,

PEs-ions and PEs-water interactions in the external potential ensemble. Deriving the CG parameters in this ensemble improves thermodynamic faithfulness and transferability across state points (e.g., salt concentrations, PE concentrations and stoichiometries) by applying spatially varying external potentials to one or more species to force local composition variations and fluctuations.[62] From the profound improvement observed in the thermodynamics of the NaCl model across concentrations (Fig. S5), we expect this strategy will also improve the quality of the PE-NaCl model. However, probing fluctuations in both PE and salt compositions will require multiple external potentials to be applied on different components, the design of which is not obvious. Thus, further investigation is necessary to find an optimal reference ensemble for coarse-graining the PE-NaCl system.

4 Conclusion and outlook

This work presents phase diagrams for a PAA/PAH complex coacervate system from a molecularly-informed field theory that captures not only the effects of charged group stoichometry, electrostatic screening with added salt, and salt partitioning behavior, but also chemistry-specific effects due to the molecular details of the polyelectrolytes (i.e., PAH-PAA asymmetries in non-stoichiometric mixtures). At the same overall PE concentration, the coacervation propensity decreases as the PAA ratio, $f_{p-} = \rho_{p-}/(\rho_{p-} + \rho_{p+})$, deviates from the stoichiometric condition ($f_{p-} = 0.5$). By reducing the number of potential ion pairs, the coacervate phase is more dilute, evidenced by shorter tie lines (Fig 4), and less salt is needed to dissolve the coacervate, resulting in a smaller two-phase region (Fig. 8A). The two-phase region shrinks at higher salinity (Fig. 6A and 8A) and the model predicts that small ions favor the dilute phase for stoichiometric mixtures (Fig. 6B). For non-stoichiometric mixtures, however, cations and anions have different partitioning patterns due to the electroneutrality constraint such that Na^+ (Cl^-) ions populate the coacervate phase when PAA (PAH) is in excess (Fig. 9). The looping-in behavior in non-stroichiometric mixtures at low salt concen-

trations, also observed previously in experiments,[77] is attributed to the competition between maximizing the translational entropy of the free ions (ions that are not neutralizing the excess charge in the coacervate) and the electroneutrality constraint in the coacervate. While the simulations do not produce quantitative agreement with the experiments they nevertheless capture qualitative trends with no fit parameters, providing an important screening tool. Nonetheless, with simple potential functional forms and assuming a constant electrostatic screening environment throughout the phase separating regimes (constant Bjerrum length), the model qualitatively captures the coacervation response to added salt concentration and mixing stoichiometries.

Atomic-scale details are extremely important in formulation and material design involving the fine-tuning of component chemistries. We believe that molecularly-informed field theories are a promising way to overcome long-standing challenges in studying coacervation physics with either 1) traditional particle-explicit models that struggle to sample meaningful conformations or 2) phenomenological field theories that lack chemical specificity. For example, it is often assumed in theoretical models that the polyanion and polycation have the same chemical structure except for opposite charges, resulting in often nonphysical symmetric phase diagrams with respect to the two PE species. We have demonstrated a bottom-up coarse-graining methodology that molecularly informs the field-theoretic model with chemical details from atomistic simulations. A notable outcome is the prediction of a non-symmetric diagram where coacervation is more favorable when the PE in excess is PAH. We believe the present coacervate model of PAA/PAH represents a significant step forward over prior simulation and theoretical studies in that it retains chemical specificity of the involved components while still making use of a computationally efficient field representation capable of rigorous phase diagram calculations.

Supporting Information Available

Supporting Information: AA forcefield validation, additional details of AA reference simulations, CG parameters, Gaussian approximation analysis and additional figures.

Acknowledgement

This work was supported by BASF Corporation through the California Research Alliance. K.T.D. and G.H.F. derived partial support from the CMMT Program of the National Science Foundation, Award DMR-2104255. Use was made of computational facilities purchased with funds from the National Science Foundation (OAC-1925717) and administered by the Center for Scientific Computing (CSC). The CSC is supported by the California NanoSystems Institute and the Materials Research Science and Engineering Center (MRSEC; NSF DMR 1720256) at UC Santa Barbara. C.E.R.E and M.E.H. were supported by the MRSEC Program of the National Science Foundation under Award No. DMR 1720256 (IRG-3).

References

(1) De Kruif, C. G.; Weinbreck, F.; de Vries, R. Complex coacervation of proteins and anionic polysaccharides. *Current opinion in colloid & interface science* **2004**, *9*, 340–349.

(2) Tolstoguzov, V. Some physico-chemical aspects of protein processing in foods. Multicomponent gels. *Food Hydrocolloids* **1995**, *9*, 317–332.

(3) Weinbreck, F.; De Vries, R.; Schrooyen, P.; De Kruif, C. Complex coacervation of whey proteins and gum arabic. *Biomacromolecules* **2003**, *4*, 293–303.

(4) Goddard, E. Polymer/surfactant interaction—its relevance to detergent systems. *Journal of the American Oil Chemists' Society* **1994**, *71*, 1–16.

(5) Wang, Q.; Dan, Y.; Wang, X. A new polymer flooding agent prepared through intermacromolecular complexation. *Journal of Macromolecular Science, Part A: Pure and Applied Chemistry* **1997**, *34*, 1155–1169.

(6) Weinbreck, F.; Minor, M.; De Kruif, C. Microencapsulation of oils using whey protein/gum arabic coacervates. *Journal of microencapsulation* **2004**, *21*, 667–679.

(7) Zhao, H.; Sun, C.; Stewart, R. J.; Waite, J. H. Cement proteins of the tube-building polychaete Phragmatopoma californica. *Journal of Biological Chemistry* **2005**, *280*, 42938–42944.

(8) Shao, H.; Bachus, K. N.; Stewart, R. J. A water-borne adhesive modeled after the sandcastle glue of P. californica. *Macromolecular bioscience* **2009**, *9*, 464–471.

(9) Stewart, R. J.; Wang, C. S.; Shao, H. Complex coacervates as a foundation for synthetic underwater adhesives. *Advances in colloid and interface science* **2011**, *167*, 85–93.

(10) Wei, W.; Tan, Y.; Rodriguez, N. R. M.; Yu, J.; Israelachvili, J. N.; Waite, J. H. A mussel-derived one component adhesive coacervate. *Acta biomaterialia* **2014**, *10*, 1663–1670.

(11) Luzzi, L. A. Microencapsulation. *Journal of pharmaceutical sciences* **1970**, *59*, 1367–1376.

(12) Klass, S. H.; Smith, M. J.; Fiala, T. A.; Lee, J. P.; Omole, A. O.; Han, B.-G.; Downing, K. H.; Kumar, S.; Francis, M. B. Self-assembling micelles based on an intrinsically disordered protein domain. *Journal of the American Chemical Society* **2019**, *141*, 4291–4299.

(13) Delcea, M.; Möhwald, H.; Skirtach, A. G. Stimuli-responsive LbL capsules and nanoshells for drug delivery. *Advanced drug delivery reviews* **2011**, *63*, 730–747.

(14) McTigue, W. C. B.; Perry, S. L. Design rules for encapsulating proteins into complex coacervates. *Soft Matter* **2019**, *15*, 3089–3103.

(15) Fares, H. M.; Ghoussoub, Y. E.; Delgado, J. D.; Fu, J.; Urban, V. S.; Schlenoff, J. B. Scattering neutrons along the polyelectrolyte complex/coacervate continuum. *Macromolecules* **2018**, *51*, 4945–4955.

(16) Bungenberg de Jong, H.; Kruyt, H. Coacervation (partial miscibility in colloid systems). Proc. K. Ned. Akad. Wet. 1929; pp 849–856.

(17) Spruijt, E., et al. Strength, structure and stability of polyelectrolyte complex coacervates. *Wageningen University, Wageningen* **2012**,

(18) Perry, S. L.; Li, Y.; Priftis, D.; Leon, L.; Tirrell, M. The effect of salt on the complex coacervation of vinyl polyelectrolytes. *Polymers* **2014**, *6*, 1756–1772.

(19) Van der Gucht, J.; Spruijt, E.; Lemmers, M.; Stuart, M. A. C. Polyelectrolyte complexes: Bulk phases and colloidal systems. *Journal of colloid and interface science* **2011**, *361*, 407–422.

(20) Priftis, D.; Laugel, N.; Tirrell, M. Thermodynamic characterization of polypeptide complex coacervation. *Langmuir* **2012**, *28*, 15947–15957.

(21) Chollakup, R.; Smitthipong, W.; Eisenbach, C. D.; Tirrell, M. Phase behavior and coacervation of aqueous poly (acrylic acid)- poly (allylamine) solutions. *Macromolecules* **2010**, *43*, 2518–2528.

(22) Chollakup, R.; Beck, J. B.; Dirnberger, K.; Tirrell, M.; Eisenbach, C. D. Polyelectrolyte Molecular Weight and Salt Effects on the Phase Behavior and Coacervation of Aqueous Solutions of Poly(acrylic acid) Sodium Salt and Poly(allylamine) Hydrochloride. *Macromolecules* **2013**, *46*, 2376–2390, DOI: 10.1021/ma202172q.

(23) Spruijt, E.; Westphal, A. H.; Borst, J. W.; Cohen Stuart, M. A.; van der Gucht, J. Binodal compositions of polyelectrolyte complexes. *Macromolecules* **2010**, *43*, 6476–6484.

(24) Li, L.; Srivastava, S.; Meng, S.; Ting, J. M.; Tirrell, M. V. Effects of non-electrostatic intermolecular interactions on the phase behavior of pH-sensitive polyelectrolyte complexes. *Macromolecules* **2020**, *53*, 7835–7844.

(25) Zhang, P.; Alsaifi, N. M.; Wu, J.; Wang, Z.-G. Polyelectrolyte complex coacervation: Effects of concentration asymmetry. *The Journal of chemical physics* **2018**, *149*, 163303.

(26) Li, L.; Srivastava, S.; Andreev, M.; Marciel, A. B.; de Pablo, J. J.; Tirrell, M. V. Phase behavior and salt partitioning in polyelectrolyte complex coacervates. *Macromolecules* **2018**, *51*, 2988–2995.

(27) Overbeek, J. T. G.; Voorn, M. Phase separation in polyelectrolyte solutions. Theory of complex coacervation. *Journal of Cellular and Comparative Physiology* **1957**, *49*, 7–26.

(28) Michaeli, I.; Overbeek, J. T. G.; Voorn, M. Phase separation of polyelectrolyte solutions. *Journal of Polymer Science* **1957**, *23*, 443–450.

(29) Mcquarrie, D. Statistical Mechanics. 1965.

(30) Doi, M.; Edwards, S. F.; Edwards, S. F. *The theory of polymer dynamics*; oxford university press, 1988; Vol. 73.

(31) Borue, V. Y.; Erukhimovich, I. Y. A statistical theory of globular polyelectrolyte complexes. *Macromolecules* **1990**, *23*, 3625–3632.

(32) Borue, V. Y.; Erukhimovich, I. Y. A statistical theory of weakly charged polyelectrolytes: fluctuations, equation of state and microphase separation. *Macromolecules* **1988**, *21*, 3240–3249.

(33) Kudlay, A.; Olvera de la Cruz, M. Precipitation of oppositely charged polyelectrolytes in salt solutions. *The Journal of chemical physics* **2004**, *120*, 404–412.

(34) Kudlay, A.; Ermoshkin, A. V.; Olvera de La Cruz, M. Complexation of oppositely charged polyelectrolytes: effect of ion pair formation. *Macromolecules* **2004**, *37*, 9231–9241.

(35) Castelnovo, M.; Joanny, J.-F. Complexation between oppositely charged polyelectrolytes: Beyond the Random Phase Approximation. *The European Physical Journal E* **2001**, *6*, 377–386.

(36) Riggleman, R. A.; Kumar, R.; Fredrickson, G. H. Investigation of the interfacial tension of complex coacervates using field-theoretic simulations. *The Journal of chemical physics* **2012**, *136*, 024903.

(37) Qin, J.; de Pablo, J. J. Criticality and connectivity in macromolecular charge complexation. *Macromolecules* **2016**, *49*, 8789–8800.

(38) Delaney, K. T.; Fredrickson, G. H. Theory of polyelectrolyte complexation—Complex coacervates are self-coacervates. *The Journal of Chemical Physics* **2017**, *146*, 224902.

(39) McCarty, J.; Delaney, K. T.; Danielsen, S. P.; Fredrickson, G. H.; Shea, J.-E. Complete phase diagram for liquid–liquid phase separation of intrinsically disordered proteins. *The journal of physical chemistry letters* **2019**, *10*, 1644–1652.

(40) Danielsen, S. P.; McCarty, J.; Shea, J.-E.; Delaney, K. T.; Fredrickson, G. H. Molecular design of self-coacervation phenomena in block polyampholytes. *Proceedings of the National Academy of Sciences* **2019**, *116*, 8224–8232.

(41) Danielsen, S. P.; McCarty, J.; Shea, J.-E.; Delaney, K. T.; Fredrickson, G. H. Small ion effects on self-coacervation phenomena in block polyampholytes. *The Journal of chemical physics* **2019**, *151*, 034904.

(42) Lee, J.; Popov, Y. O.; Fredrickson, G. H. Complex coacervation: A field theoretic simulation study of polyelectrolyte complexation. *The Journal of chemical physics* **2008**, *128*, 224908.

(43) Popov, Y. O.; Lee, J.; Fredrickson, G. H. Field-theoretic simulations of polyelectrolyte complexation. *arXiv preprint arXiv:0705.0718* **2007**,

(44) Shen, K.; Wang, Z.-G. Polyelectrolyte chain structure and solution phase behavior. *Macromolecules* **2018**, *51*, 1706–1717.

(45) Fredrickson, G., et al. *The equilibrium theory of inhomogeneous polymers*; Oxford University Press on Demand, 2006; Vol. 134.

(46) Fredrickson, G. H.; Ganesan, V.; Drolet, F. Field-theoretic computer simulation methods for polymers and complex fluids. *Macromolecules* **2002**, *35*, 16–39.

(47) Lennon, E. M.; Mohler, G. O.; Ceniceros, H. D.; García-Cervera, C. J.; Fredrickson, G. H. Numerical solutions of the complex Langevin equations in polymer field theory. *Multiscale Modeling & Simulation* **2008**, *6*, 1347–1370.

(48) Fredrickson, G. H.; Delaney, K. T. Direct free energy evaluation of classical and quantum many-body systems via field-theoretic simulation. *Proceedings of the National Academy of Sciences* **2022**, *119*, e2201804119.

(49) Audus, D. J.; Gopez, J. D.; Krogstad, D. V.; Lynd, N. A.; Kramer, E. J.; Hawker, C. J.; Fredrickson, G. H. Phase behavior of electrostatically complexed polyelectrolyte gels using an embedded fluctuation model. *Soft Matter* **2015**, *11*, 1214–1225.

(50) Perry, S. L.; Sing, C. E. Prism-based theory of complex coacervation: Excluded volume versus chain correlation. *Macromolecules* **2015**, *48*, 5040–5053.

(51) Wallin, T.; Linse, P. Monte Carlo simulations of polyelectrolytes at charged micelles. 1. Effects of chain flexibility. *Langmuir* **1996**, *12*, 305–314.

(52) Liu, Z.; Shang, Y.; Feng, J.; Peng, C.; Liu, H.; Hu, Y. Effect of hydrophilicity or hydrophobicity of polyelectrolyte on the interaction between polyelectrolyte and surfactants: molecular dynamics simulations. *The Journal of Physical Chemistry B* **2012**, *116*, 5516–5526.

(53) Lou, J.; Friedowitz, S.; Qin, J.; Xia, Y. Tunable coacervation of well-defined homologous polyanions and polycations by local polarity. *ACS central science* **2019**, *5*, 549–557.

(54) Sherck, N.; Shen, K.; Nguyen, M.; Yoo, B.; Kohler, S.; Speros, J. C.; Delaney, K. T.; Shell, M. S.; Fredrickson, G. H. Molecularly Informed Field Theories from Bottom-up Coarse-Graining. *ACS Macro Letters* **2021**, *10*, 576–583.

(55) Shell, M. S. The relative entropy is fundamental to multiscale and inverse thermodynamic problems. *The Journal of chemical physics* **2008**, *129*, 144108.

(56) Chaimovich, A.; Shell, M. S. Relative entropy as a universal metric for multiscale errors. *Physical Review E* **2010**, *81*, 060104.

(57) Shell, M. S. Coarse-graining with the relative entropy. *Advances in chemical physics* **2016**, *161*, 395–441.

(58) Sanyal, T.; Shell, M. S. Coarse-grained models using local-density potentials optimized with the relative entropy: Application to implicit solvation. *The Journal of chemical physics* **2016**, *145*, 034109.

(59) Suda, M.; Okubo, T. The influence of pH on the alternate multi-layered adsorption of macrocations and macroanions on colloidal spheres. *Colloid and Polymer Science* **2004**, *282*, 518–523.

(60) Bhatia, S. R.; Khattak, S. F.; Roberts, S. C. Polyelectrolytes for cell encapsulation. *Current opinion in colloid & interface science* **2005**, *10*, 45–51.

(61) Rathee, V. S.; Zervoudakis, A. J.; Sidky, H.; Sikora, B. J.; Whitmer, J. K. Weak polyelectrolyte complexation driven by associative charging. *The Journal of Chemical Physics* **2018**, *148*, 114901.

(62) Shen, K.; Sherck, N.; Nguyen, M.; Yoo, B.; Köhler, S.; Speros, J.; Delaney, K. T.; Fredrickson, G. H.; Shell, M. S. Learning composition-transferable coarse-grained models: Designing external potential ensembles to maximize thermodynamic information. *The Journal of Chemical Physics* **2020**, *153*, 154116.

(63) Izadi, S.; Anandakrishnan, R.; Onufriev, A. V. Building water models: a different approach. *J. Phys. Chem. Lett.* **2014**, *5*, 3863–3871.

(64) Joung, I. S.; Cheatham III, T. E. Determination of alkali and halide monovalent ion parameters for use in explicitly solvated biomolecular simulations. *The journal of physical chemistry B* **2008**, *112*, 9020–9041.

(65) Wang, J.; Wolf Romain, M.; Caldwell James, W.; Kollman Peter, A.; Case David, A. Development and testing of a general amber force field. *Journal of Computational Chemistry* **2004**, *25*, 1157–1174, DOI: 10.1002/jcc.20035.

(66) Wang, J.; Cieplak, P.; Kollman, P. A. How well does a restrained electrostatic potential (RESP) model perform in calculating conformational energies of organic and biological molecules? *Journal of computational chemistry* **2000**, *21*, 1049–1074.

(67) Frisch, M. J. et al. Gaussian˜16 Revision C.01. 2016; Gaussian Inc. Wallingford CT.

(68) Eastman, P.; Swails, J.; Chodera, J. D.; McGibbon, R. T.; Zhao, Y.; Beauchamp, K. A.; Wang, L.-P.; Simmonett, A. C.; Harrigan, M. P.; Stern, C. D., et al. OpenMM 7: Rapid development of high performance algorithms for molecular dynamics. *PLoS computational biology* **2017**, *13*, e1005659.

(69) Suter, U. W. Epimerization of vinyl polymers to stereochemical equilibrium. 1. Theory. *Macromolecules* **1981**, *14*, 523–528.

(70) Gupta, A. K.; Natarajan, U. Tacticity effects on conformational structure and hydration of poly-(methacrylic acid) in aqueous solutions-a molecular dynamics simulation study. *Molecular Simulation* **2016**, *42*, 725–736.

(71) Bertsekas, D. P. *Constrained optimization and Lagrange multiplier methods*; Academic press, 2014.

(72) Powell, M. J. Algorithms for nonlinear constraints that use Lagrangian functions. *Mathematical programming* **1978**, *14*, 224–248.

(73) Gould, N. I. M. On the convergence of a sequential penalty function method for constrained minimization. *SIAM Journal on Numerical Analysis* **1989**, *26*, 107–128.

(74) Cranford, S. W.; Buehler, M. J. Variation of weak polyelectrolyte persistence length through an electrostatic contour length. *Macromolecules* **2012**, *45*, 8067–8082.

(75) Mintis, D. G.; Mavrantzas, V. G. Effect of pH and molecular length on the structure and dynamics of short poly (acrylic acid) in dilute solution: Detailed molecular dynamics study. *The Journal of Physical Chemistry B* **2019**, *123*, 4204–4219.

(76) Panagiotopoulos, A. Z.; Quirke, N.; Stapleton, M.; Tildesley, D. Phase equilibria by simulation in the Gibbs ensemble: alternative derivation, generalization and application to mixture and membrane equilibria. *Molecular Physics* **1988**, *63*, 527–545.

(77) Friedowitz, S.; Lou, J.; Barker, K. P.; Will, K.; Xia, Y.; Qin, J. Looping-in complexation and ion partitioning in nonstoichiometric polyelectrolyte mixtures. *Science Advances* **2021**, *7*, eabg8654.

(78) Neitzel, A. E.; Fang, Y. N.; Yu, B.; Rumyantsev, A. M.; de Pablo, J. J.; Tirrell, M. V.

Polyelectrolyte complex coacervation across a broad range of charge densities. *Macromolecules* **2021**, *54*, 6878–6890.

(79) Luo, Y.; Gu, M.; Edwards, C. E.; Valentine, M. T.; Helgeson, M. E. High-throughput microscopy to determine morphology, microrheology, and phase boundaries applied to phase separating coacervates. *Soft Matter* **2022**, *18*, 3063–3075.

(80) Zhang, P.; Alsaifi, N. M.; Wu, J.; Wang, Z.-G. Salting-out and salting-in of polyelectrolyte solutions: A liquid-state theory study. *Macromolecules* **2016**, *49*, 9720–9730.

(81) Grzetic, D. J.; Delaney, K. T.; Fredrickson, G. H. Contrasting dielectric properties of electrolyte solutions with polar and polarizable solvents. *Physical review letters* **2019**, *122*, 128007.